Downloaded via UNIV OF VIRGINIA on February 1, 2024 at 19:25:00 (UTC). See https://pubs.acs.org/sharingguidelines for options on how to legitimately share published articles.



www.acsnano.org

Reconfigurable Physical Reservoir in GaN/α - In_2Se_3 HEMTs Enabled by Out-of-Plane Local Polarization of Ferroelectric 2D Layer

Jeong Yong Yang, Minseong Park, Min Jae Yeom, Yongmin Baek, Seok Chan Yoon, Yeong Je Jeong, Seung Yoon Oh, Kyusang Lee,* and Geonwook Yoo*



Cite This: ACS Nano 2023, 17, 7695-7704



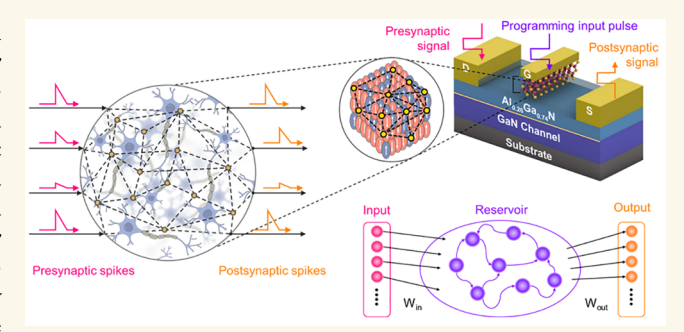
ACCESS

Metrics & More

Article Recommendations

s Supporting Information

ABSTRACT: Significant effort for demonstrating a gallium nitride (GaN)-based ferroelectric metal—oxide—semiconductor (MOS)-high-electron-mobility transistor (HEMT) for reconfigurable operation via simple pulse operation has been hindered by the lack of suitable materials, gate structures, and intrinsic depolarization effects. In this study, we have demonstrated artificial synapses using a GaN-based MOS-HEMT integrated with an α -In₂Se₃ ferroelectric semiconductor. The van der Waals heterostructure of GaN/ α -In₂Se₃ provides a potential to achieve high-frequency operation driven by a ferroelectrically coupled two-dimensional electron gas (2DEG). Moreover, the semiconducting α -In₂Se₃ features a steep subthreshold slope



with a high ON/OFF ratio ($\sim 10^{10}$). The self-aligned α -In₂Se₃ layer with the gate electrode suppresses the in-plane polarization while promoting the out-of-plane (OOP) polarization of α -In₂Se₃, resulting in a steep subthreshold slope (10 mV/dec) and creating a large hysteresis (2 V). Furthermore, based on the short-term plasticity (STP) characteristics of the fabricated ferroelectric HEMT, we demonstrated reservoir computing (RC) for image classification. We believe that the ferroelectric GaN/ α -In₂Se₃ HEMT can provide a viable pathway toward ultrafast neuromorphic computing.

KEYWORDS: GaN/α -In₂Se₃ heterostructure, ferroelectric semiconductor, polarization, self-aligned structure, reservoir computing

allium nitride (GaN) high-electron-mobility transistors (HEMTs) are attractive for high-frequency applications owing to their high electron mobility (>2000 cm²/(V s)).¹⁻⁴ Recently, ferroelectric-based GaN metal-oxide-semiconductor (MOS) HEMTs using HZO, PZT, and HfO₂ dielectrics have been proposed to reduce the device dimensions and achieve lower power consumption via a negative capacitance effect. 5-13 However, it has been still challenging for ferroelectric-GaN MOS-HEMTs to achieve ideal performance of a large hysteresis (ΔV) and low subthreshold slope (SS) owing to the depolarization effect caused by the interface charge trapping and polarization of the AlGaN barrier layer. $^{14-16}$ To maximize the ΔV and steep SS, the integration of a ferroelectric material with strong ferroelectric polarization and without dangling bonds is ideal for ferroelectric-GaN MOS-HEMTs. Therefore, in this study, we employed a highly crystalline two-dimensional (2D) ferroelectric material, α -In₂Se₃, as a ferroelectric gate heterostructure in GaN MOS-HEMTs because it is free from the charge-trapping effect in dangling bonds and has a high carrier concentration. The α -In₂Se₃ exhibits both ferroelectric

and semiconducting characteristics.^{17–19} Thus, it provides a fast speed barrier height modulation along with a relatively robust activity against a depolarization field.^{17–24}

Moreover, the enhancement of the vertical polarization in the ferroelectric layer was achieved by developing a self-aligned structure between the gate electrode and $\alpha\text{-In}_2\mathrm{Se}_3$, which suppresses the polarization in the lateral directions. The effectiveness of the aligned structure was also verified using physics-based technology computer aided design (TCAD) simulations. To prove the ferroelectric polarization effect in the $\mathrm{GaN}/\alpha\text{-In}_2\mathrm{Se}_3$ MOS-HEMT structure, we demonstrated modulation of the effective Schottky barrier height $(\Delta\Phi_{\mathrm{eff}})$ in the $\mathrm{GaN}/\alpha\text{-In}_2\mathrm{Se}_3$ metal—semiconductor—HEMT (MES-

Received: January 6, 2023 Accepted: March 30, 2023 Published: April 4, 2023





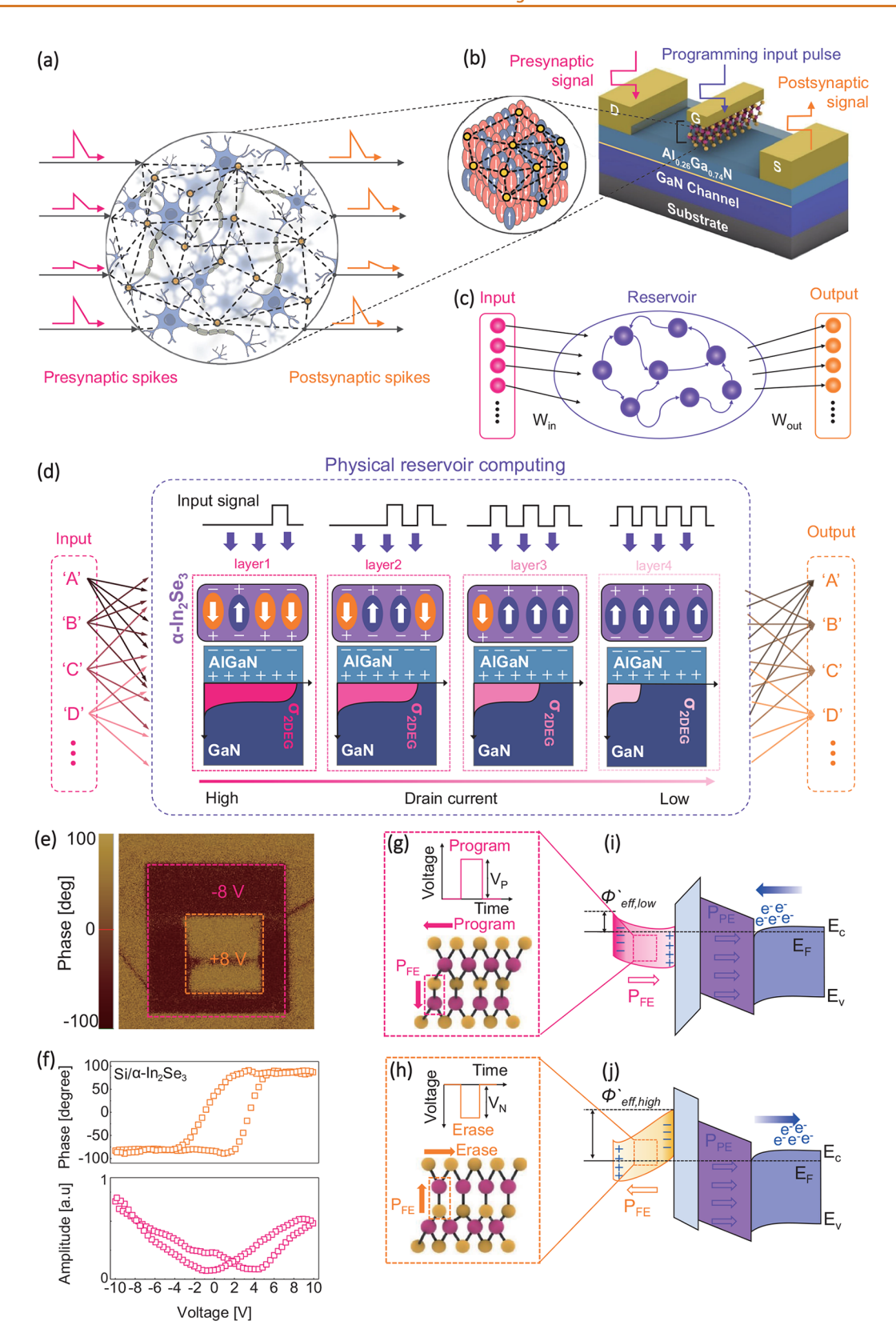


Figure 1. (a) Illustration of presynaptic and postsynaptic schematic of the emulated neuron system in reservoir computing (RC) and (b) the 3D schematic image of fabricated devices. (c) Schematic illustration of the RC process. (d) The schematic of the physical RC process based on the GaN/ferroelectric-semiconductor heterostructure. (e) A scanned piezoelectric force measurement (PFM) phase image after applying a bias of +8 V and -8 V, sequentially. (f) The amplitude and phase graph versus external tip bias measured on an α -In₂Se₃/Si substrate. The atomic structure of α -In₂Se₃ and pulse scheme for the (g) program and (h) erase states. (i) and (j) show a band diagram of the fabricated device under program and erase states, respectively.

HEMT) structure. Hence, superior SS characteristics of ~ 10 mV/dec and a ΔV of ~ 2 V were achieved using the GaN/ α -In₂Se₃ MOS HEMT compared to conventional oxide-based ferroelectic GaN MOS-HEMTs.²⁵

Accordingly, neuromorphic computing, which is an emerging computing architecture that uses artificial synapses for a massive amount of information processing, is considered to be suitable application of GaN/α -In₂Se₃ MOS-HEMT.^{26,27} Especially, among the neuromorphic architectures, reservoir computing (RC) is well known for being suitable for processing temporal data and data with high dimensionality. 28-30 The RC process, which mimics the biological shortterm plasticity (STP), allows for a nonlinear encoding framework in a time domain, reducing the data dimensionality without the need for additional training processes.3 Furthermore, to maximize the performance of neuromorphic computing for the in situ processing of big data in hardware, it is desirable to achieve fast-switching operation of artificial synapses. Therefore, the GaN/α -In₂Se₃ MOS-HEMT was characterized as an artificial synapse for neuromorphic applications. Biological STP is realized by the spontaneous relaxation of excitatory postsynaptic current (EPSC). We believe that this study implies that the GaN/α-In₂Se₃ heterostructure based MOS-HEMT has the potential to be employed in high-speed neuromorphic computing applications.

RESULTS

GaN/α-In₂Se₃ Heterostructure and Ferroelectric HEMT Operation. Figure 1a illustrates presynaptic and postsynaptic processes in RC, in which each neuron is randomly connected in the reservoir layer. The structure of the GaN/α-In₂Se₃ MOS-HEMT, which mimics the biological synapse between presynaptic and postsynaptic neurons, is schematically shown in Figure 1b. To achieve short- and longterm synaptic plasticity in the human brain, accumulated sequential input potentials trigger the action potential to drive postsynaptic spikes. Similar to the biological synapse, the transconductance of the GaN/α -In₂Se₃ MOS-HEMT can serve as the synaptic weight, and the presynaptic and postsynaptic spikes can be emulated as the input pulse and output current to and from the source and drain electrodes of the GaN/α -In₂Se₃ MOS-HEMT, respectively. Figure 1c illustrates the schematic of the RC employed in this study for image classification by processing the input data through a randomly assigned reservoir layer. The randomly interconnected reservoir layer allows the nonlinear encoding of the input dimension without additional training processes, and the encoded output can be further utilized as a classification task. Figure 1d shows an illustration of the physical RC process using the GaN/α-In₂Se₃ MOS-HEMT by coupling the partial ferroelectric polarization of α-In₂Se₃ with two-dimensional electron gas (2DEG) in the channel. Here, the partial ferroelectric polarization of α -In₂Se₃ is introduced by the electrical pulse to the gate electrode, which can be accumulated and shows the temporal relaxation that mimics the biological

Figure 1e shows the piezo-response force microscopy (PFM) mapping for out-of-plane (OOP, vertical) polarizations of α -In₂Se₃ by applying a sequential bidirectional DC bias of +8 V and -8 V. The OOP and in-plane (IP, lateral) ferroelectric polarizations of α -In₂Se₃ are switched simultaneously via an external electric field, resulting in a dipole-

locking effect.³² However, the OOP ferroelectric polarization of α -In₂Se₃ dominantly affects the channel conductance of the GaN/α-In₂Se₃ MOS-HEMT as a gate structure. Figure 1f shows the amplitude and phase responses to the application of external voltages, confirming the clear transition of the polarization above the coercive field. The ferroelectricity of layered α -In₂Se₃ originates from the shift of the Se atom by an external electric field, as shown in Figure 1g and h. Using the ferroelectric property of α-In₂Se₃, we have demonstrated a GaN/α - In_2Se_3 MOS-HEMT that exhibits output current states. The application of positive (for program, V_p) and negative (for erase, V_N) pulses to the gate electrode tunes the ferroelectric polarization of the α -In₂Se₃ layer coupled with the V_P channel in the GaN MOS-HEMT. The multilayer ferroelectric polarization switching characteristic of α-In₂Se₃ allows the emulation of biological STP. Specifically, STP behavior can be achieved by the local polarization of the α -In₂Se₃ membrane, offering RC capability. In conjunction with high-frequency operation, the heterogeneously integrated GaN/α -In₂Se₃ MOS-HEMT serves as a single synapse. Figure 1i shows the band diagram of the GaN/α -In₂Se₃ MOS-HEMT heterostructure with the application of a programming pulse, where $\Phi'_{\rm eff}$ indicates the effective barrier height through the α - In_2Se_3 layer. The V_P leads to the alignment of the ferroelectric polarization in the same direction as the polarization in the AlGaN barrier (P_{PE}). Therefore, carriers in the AlGaN/GaN 2DEG channel accumulate when the conduction band is lowered below the Fermi level. With the application of V_N , the ferroelectric polarization is aligned in the opposite direction of the P_{PE} , which counters the polarization in the AlGaN barrier. Thus, the conduction band in the heterostructure rises above the Fermi level, and the carriers in the 2DEG channel are fully depleted, as shown in Figure 1j. Furthermore, the accumulation and depletion of carriers within the semiconducting α - In_2Se_3 layer depending on applied gate bias modulate the Φ'_{eff} inducing the depletion capacitance (C_{dep}) at the interface of α - In_2Se_3/Al_2O_3 .

Schottky Barrier Modulation in GaN/α -In₂Se₃ via Ferroelectric Polarization. Unlike conventional ferroelectric insulators, α -In₂Se₃ is a semiconductor material; thus, the P-Ecurve cannot be measured directly.¹⁸ Instead, the ferroelectricity of α-In₂Se₃ can be verified by observing the modulation of the effective barrier height $(\Delta\Phi_{\rm eff})$ in the GaN/ α -In₂Se₃ MES-HEMT. Thus, to elucidate the repercussions of ferroelectric polarization and the mechanism of $\Delta\Phi_{\mathrm{eff}}$ a GaN/lpha-In₂Se₃ MES-HEMT was fabricated and investigated, as shown in Figure S1a. Figure S1b presents the transfer curve under a forward sweep after the application of V_N and V_P pulses. The off-current under the application of gate bias is governed by $\Delta\Phi_{
m eff}$ since the gate leakage increases with the decrease of $\Phi_{
m eff}$. In metal/ α -In $_2$ Se $_3$ /semiconductor layer stacks, $\Delta\Phi_{\mathrm{eff}}$ can be enhanced by the depletion effect of the semiconductor region. Figure S1c shows the band diagram of the GaN/α -In₂Se₃ MES-HEMT after the application of a negative pulse. The negative pulse rearranges the ferroelectric polarization in α -In₂Se₃, which counters the polarization of the AlGaN layer. Consequently, $\Phi_{\rm eff}$ increases after applying a negative pulse, preventing electrons from being injected into the 2DEG from the gate. The positive pulse aligns the ferroelectric polarization in the same direction as the AlGaN polarization. Thus, it lowers Φ_{eff} and the gate leakage increases as shown in Figure S1d. To extract $\Delta \Phi_{\text{eff}}$ at the GaN/ α -In₂Se₃ MES-HEMT structure, we plotted a gate leakage model through linearity

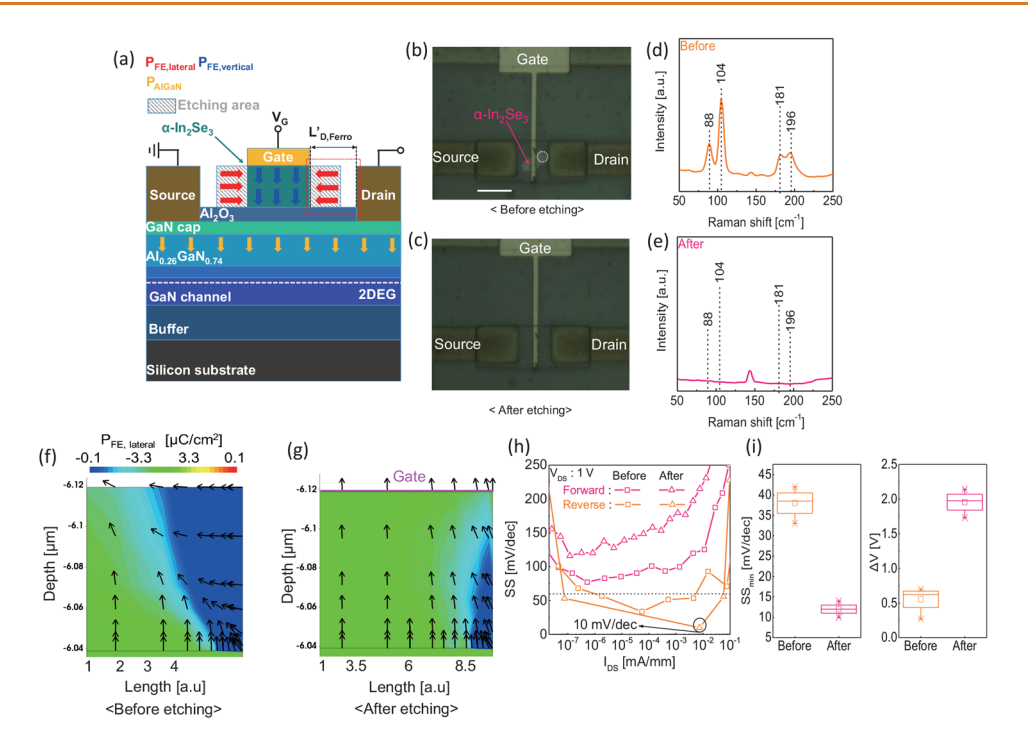


Figure 2. (a) A cross-section schematic of GaN/α -In₂Se₃ MOS-HEMT before and after the etching process. (b and c) Optical microscopy image of the region where Raman spectroscopy analysis was conducted on α -In₂Se₃ before and after the etching process (white dashed circle); the scale bar is $10 \, \mu \text{m}$. (d and e) The corresponding Raman peaks of α -In₂Se₃. (f and g) Technology computer aided design (TCAD) simulation results on α -In₂Se₃ before and after the etching process. Color charts and arrows indicate the lateral polarization and vector of total polarization, which shows the area marked as a red dashed box in (a). (h) Subthreshold slope (SS) vs drain current (I_{DS}) plot of the GaN/α -In₂Se₃ MOS-HEMT before and after the etching process at forward and reverse sweep. (i) Extracted minimum subthreshold slope (SS_{min}) and hysteresis (ΔV) graph of GaN/α -In₂Se₃ MOS-HEMT for five devices before and after the etching process.

fitting into the measured gate current to confirm compatibility for the thermionic and diffusion model, as shown in Figure S1e and f. Based on the verification of precondition for using the thermionic and diffusion model, the current flow through the α -In₂Se₃ is described as below.³³

$$I = A'A^{**}T^{2}\exp\left(-\frac{\Phi_{\rm r}}{kT}\right)\exp\left(\frac{q\sqrt{q\xi/4\pi k_{\rm s}}}{kT}\right),$$

$$\xi = \sqrt{\frac{2qN_{\rm D}}{k_{\rm s}}}\left(V + V_{\rm bi} - \frac{kT}{q}\right)$$
(1)

where A' is the area of the barrier-height region, A^{**} is the effective Richardson constant, q is the electron charge, $N_{\rm D}$ is the donor impurity density, and $k_{\rm s}$ is the permittivity of α -In₂Se₃. With A', A^{**} , $K_{\rm s}$, T, and $V_{\rm bi}$ being constants, the approximation of $\Delta\Phi_{\rm eff}$ can be obtained from the subtraction of ln(I) before and after applying gate pulse. Consequently, $\Delta\Phi_{\rm eff}$ was calculated using eq 2 using a different pulse amplitude, indicating clear evidence of ferroelectric polarization in α -In₂Se₃ as shown in Figure S1g.

$$\ln[I(P)/I(0)] \sim -\Delta\Phi_{\text{eff}}/kT \tag{2}$$

where I(0) and I(P) are the gate leakages before and after the application of a pulse to the gate metal, respectively, k indicates the Boltzmann constant, and T is the temperature. (For more detail, see the explanation in Figure S1.)

Geometrical Design by Self-Aligned Gate Structure. To maximize the ferroelectric effect on the coupled 2DEG channel, we confined the α -In₂Se₃ area by selectively removing the film outside the gate metal region through a wet-etching

process. For the GaN/α -In₂Se₃ MOS-HEMT structure without a confined α -In₂Se₃ layer, the area of α -In₂Se₃ adjacent to the drain electrode was unintentionally polarized owing to the drain bias. Thus, when a $V_{
m N}$ and $V_{
m P}$ are applied to the gate electrode to align the polarization, the induced parasitic polarization from the drain bias offsets the polarization derived via the gate pulse. Therefore, this limits the ferroelectric polarization of the GaN/α -In₂Se₃ MOS-HEMT in the OOP direction. Herein, we constrained the unwanted parasitic IP polarization by self-defining the area of α -In₂Se₃ matching with the gate electrode. Figure 2a shows a schematic of the GaN/α - In_2Se_3 MOS-HEMT before and after confining the α - In_2Se_3 layer, where the gray dashed box represents the etched area. The red and blue arrows indicate IP and OOP polarizations in the α -In₂Se₃ layer, respectively. The $L'_{D,Ferro}$ (4.5 μ m) is the length between the α-In₂Se₃ and drain metal after the selfdefined wet etching process. Optical microscopy images of the device before and after the self-defined etching process are shown in Figure 2b and c. The corresponding Raman peaks of the α -In₂Se₃ etched area were negligible after the etching process, indicating that α -In₂Se₃ was completely removed by wet etching, as shown in Figure 2d and e. 17,34

The 2DEG was depleted when the ferroelectric polarization was contrary to the polarization of the AlGaN barrier layer (yellow arrows in Figure 2a). We performed TCAD (Synopsys Corp.) simulation using an experimentally calibrated model before and after the etching process to verify the effect of polarization concentration, as shown in Figure 2f and g. The bandgap energies of GaN, AlGaN, Al₂O₃, and α -In₂Se₃ utilized for TCAD simulation are 3.4, 4.0, 6.4, and 1.39 eV, respectively; furthermore, corresponding electron affinities

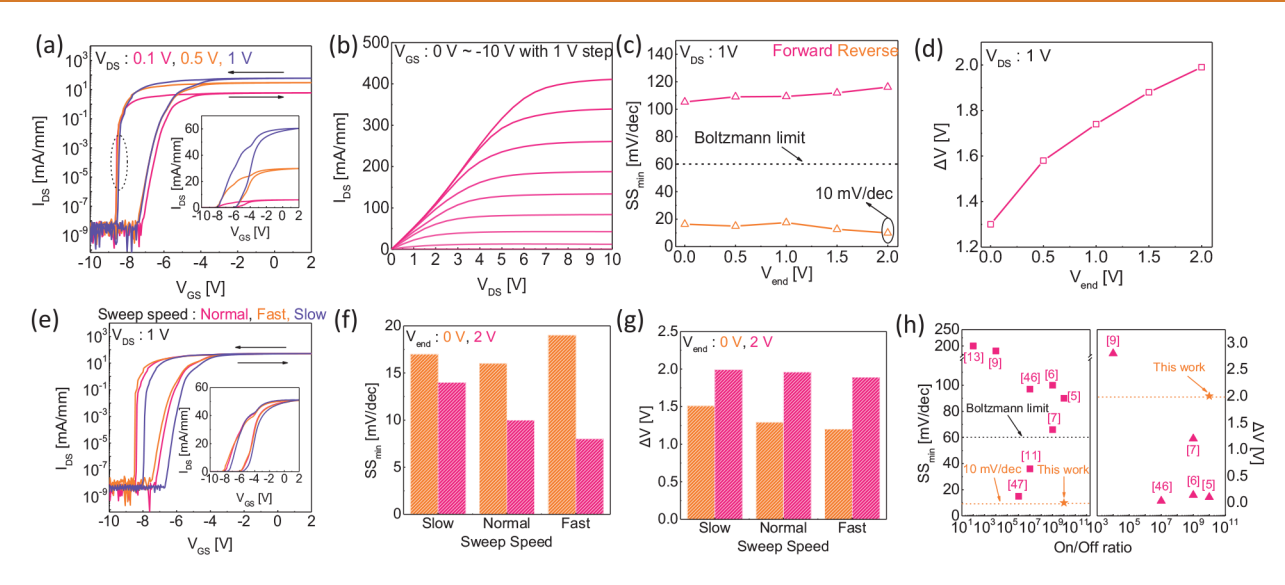


Figure 3. (a) Normalized bidirectional $I_{\rm DS}$ vs gate voltage $(V_{\rm GS})$ transfer curve of GaN/ α -In₂Se₃ MOS-HEMT at drain voltage $(V_{\rm DS})=0.1$, 0.5, and 1 V, respectively. The inset shows the linear scale of the bidirectional curve of (a). (b) Normalized $I_{\rm DS}$ vs $V_{\rm DS}$ output curve of GaN/ α -In₂Se₃ MOS-HEMT at a $V_{\rm GS}$ range of 0 to -10 V. (c and d) $SS_{\rm min}$ and ΔV versus different $V_{\rm GS}$ sweep ranges. Parameters were extracted from the bidirectional $I_{\rm DS}$ vs $V_{\rm GS}$ transfer curve of GaN/ α -In₂Se₃ MOS-HEMT. (e) Bidirectional $I_{\rm DS}$ vs $V_{\rm GS}$ transfer curve of GaN/ α -In₂Se₃ MOS-HEMT at $V_{\rm DS}=1$ V, measured under a slow, normal, and fast sweep speed mode. (f and g) $SS_{\rm min}$ and ΔV extracted from Figure 3e at $V_{\rm end}=0$, 2 V under a slow, normal, and fast sweep speed. (h) A benchmark plot of $SS_{\rm min}$ and ΔV versus ON/OFF ratio of $SS_{\rm MOS-HEMT}$ compared with other previous works. $S_{\rm T}=0.11$, $S_{\rm T}=0.11$,

are 4.1, 4.6, 1.35, and 3.6 eV. 35-41 The arrows in Figure 2f and g indicate the vectors of the total polarization in α -In₂Se₃, whereas the color chart shows the magnitude of the lateral polarization. The simulation confirmed that lateral polarization was suppressed when the α-In₂Se₃ layer was self-aligned with the gate metal, while the total polarization was preserved. Moreover, a bidirectional transfer curve was measured before and after the confining process to verify the improved SS originating from the enhanced ferroelectric polarization effect. 42,43 Figure 2h shows the SS extracted from the bidirectional transfer curve before and after the etching process. After the etching process, the initial ferroelectric polarization in the reverse OOP direction of the confined α -In₂Se₃ polled by the polarization of the AlGaN barrier layer becomes stronger. Consequently, the SS under the forward sweep increased. In contrast, the SS under backward sweep was significantly reduced after the etching process because the ferroelectric polarization was aligned more strongly in the same direction as the AlGaN barrier layer. Therefore, we were able to achieve the average minimum value of SS (SS_{min}) and ΔV as low as 15 mV/dec and 2 V for five devices, respectively, via a self-aligned α-In₂Se₃-based ferroelectric GaN MOS-HEMT structure, as shown in Figure 2i and Figure S2. Such devices with steep SS can be effectively used for low power consumption circuits including spiking neural network applications.

Electrical Performance of Ferroelectric GaN/ α **-In**₂Se₃ **MOS-HEMT.** Figure 3a shows the bidirectional transfer curves at drain voltages (V_{DS}) of 0.1, 0.5, and 1 V; the inset of Figure 3a shows the identical curve in linear scale. Counterclockwise ΔV is referred to as switching of the ferroelectric polarization of α -In₂Se₃ in the GaN/ α -In₂Se₃ MOS-HEMT structure. To confirm the output characteristics of the GaN/ α -In₂Se₃ MOS-HEMT, we measured the I_{DS} vs V_{DS} output curve for the V_{GS} range from 0 V to -10 V with a 1 V step, as shown in Figure 3b. Furthermore, the SS_{\min} and ΔV under various V_{GS} sweep

ranges ($V_{\rm end}$ indicate the end point of $V_{\rm GS}$ sweep range), -10 to 0 V and -10 to 2 V, were extracted from the bidirectional transfer curve at $V_{\rm DS}=1$ V. Steep SS in ferroelectric-FET (FeFET) is advantageous for neuromorphic computing applications because it minimizes the power consumption by preventing unwanted switching behavior until it reaches the threshold voltage. Specifically, the low subthreshold current suppresses the leakage current generated by a sequential input pulse train. ⁴⁴ Figure 3c shows $SS_{\rm min}$ vs $V_{\rm end}$ for the forward and reverse sweeps.

The SS_{min} is maintained below 20 mV/dec at a V_{end} range from 0 to 2 V, and it is decreased further to 10 mV/dec when $V_{\rm end}$ = 2 V. Subsequently, the bidirectional $I_{\rm DS}$ vs $V_{\rm GS}$ curve was measured to observe the switching behavior of ferroelectricity in α -In₂Se₃ by an external electric field, thus varying the start and end point of the V_{GS} sweep range as shown in Figure S3a and b. Owing to the coercive field (for both negative and positive amplitude) in α -In₂Se₃, as confirmed in PFM data, the direction of ferroelectric polarization can be flipped by an external electric field. Figure 3d exhibits the ΔV graph extracted from the transfer curve for V_{end} from 0 to 2 V, indicating a gate sweep range (from -10 to 2 V) sufficiently induces ferroelectricity of α -In₂Se₃. Furthermore, the impact of the thickness and area of α -In₂Se₃ is assessed, as depicted in Figure S3c and d; both ΔV and SS are improved due to enhanced ferroelectrically coupled 2DEG controllability.

In addition to the gate-aligned HEMT structure promoting out-of-plane polarization, the record low $SS_{\rm min}$ in backward sweep can be achieved by the additional $C_{\rm dep}$ within the ferroelectric $\alpha\text{-In}_2\mathrm{Se}_3$ semiconductor layer. The equivalent circuit of a typical ferroelectric MOS-HEMT is a series combination of $C_{\rm pol}-C_{\rm ins}-C_{\rm AlGaN}-C_{\rm GaN}$ without $C_{\rm dep}$, where $C_{\rm pol}$ and $C_{\rm ins}$ are the capacitances of the ferroelectric polarization and dielectric layer, respectively. Then, the extracted SS can be expressed as below:

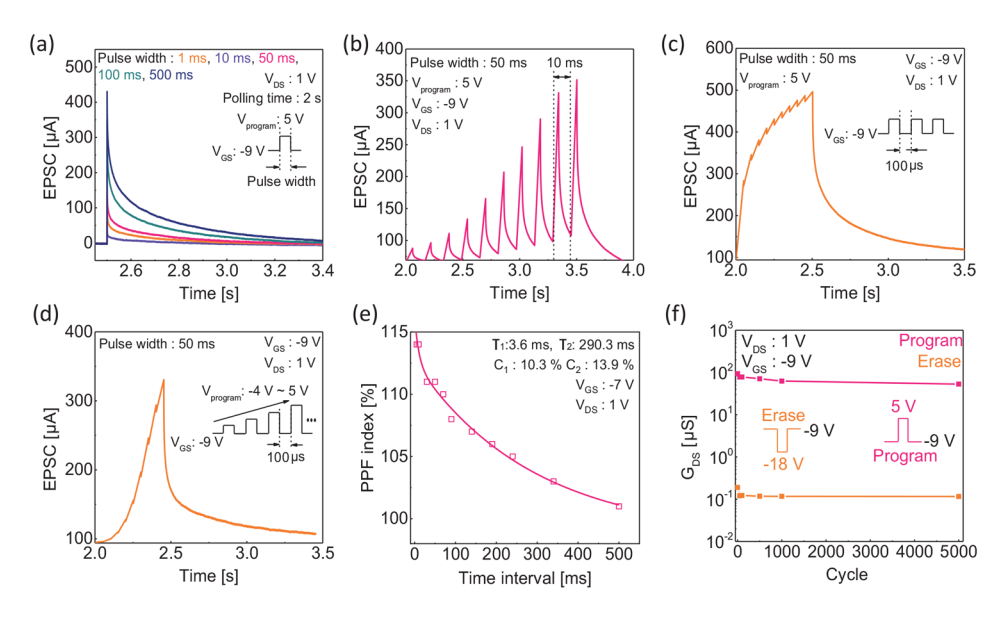


Figure 4. (a) Excitatory postsynaptic current (EPSC) responses for different gate input widths from 1 to 500 ms. Each output current of the EPSC is collected from the drain electrode of the GaN/α -In₂Se₃ MOS-HEMT while the input pulses are applied to the gate electrode. Cumulative EPSC responses for sequential pulses with a time interval of (b) 10 ms and (c) 100 μ s and (d) with incremental amplitudes. (e) For various time intervals between two sequential pulses, ranging from 10 to 500 ms, the pair-pulse facilitation (PPF) was calculated from 1st and 2nd peaks of each EPSC. (f) Endurance cycle for the program and erase operations. Response current was measured after applying program and erase pulses at $V_{DS} = 1$ V.

$$SS = 60 \left(1 + \frac{C_{\text{HEMT}}}{C_{\text{ins}}} \right) \left(1 - \frac{C_{\text{MOS}}}{|C_{\text{pol}}|} \right),$$

$$C_{\text{MOS}} = \frac{C_{\text{HEMT}} C_{\text{ins}}}{C_{\text{HEMT}} + C_{\text{ins}}}$$
(3)

$$\frac{1}{A_{\rm V}} = \left(1 - \frac{C_{\rm MOS}}{|C_{\rm pol}|}\right) \tag{4}$$

The term $\left(1 - \frac{C_{\text{MOS}}}{|C_{\text{pol}}|}\right)$ in eq 3 indicates that ferroelectric polarization can further decrease the SS below 60 mV/dec. Specifically, the term $\left(1-\frac{C_{MOS}}{|C_{pol}|}\right)$ is associated with voltage amplification (A_V), and the term $1/A_V$ can be described as shown in eq 4. Under a specific condition $(C_{ins} > |C_{pol}|)$, $1/A_V$ has a value of less than 1, which is mainly attributed to the polarization switching in α -In₂Se₃.³⁵ $C_{\rm ins}$ of 1.593 \times 10⁻⁶ F/cm² and $C_{\rm pol}$ of \sim 0.2 \times 10⁻⁶ F/cm² are extracted from C-Vmeasurement using the fabricated MOSCAP and through the TCAD simulation, respectively. By comparing C_{ins} and C_{pol} , we confirmed that the condition of $C_{\text{ins}} > |C_{\text{pol}}|$ for proving $1/A_{\text{V}} <$ 1 is satisfied, and the SS below 60 mV/dec at room temperature can be explained using eqs 3 and 4.43 In addition to the ferroelectric polarization effect, reduction in C_{pol} by adding a series capacitance results in a further decrease in the SS. Applying an erase pulse (i.e., a backward sweep) induces additional C_{dep} within the $lpha\text{-In}_2\text{Se}_3$ layer, and C_{pol} can be expressed as a series capacitance of C_{pol} and C_{dep} as shown in Figure S3c and d. Thus, the term $\left(1 - \frac{C_{MOS}}{|C_{mol}|}\right)$ in eq 3 is

expressed as below:

$$\frac{1}{A'_{V}} = \left(1 - \frac{C_{MOS}}{\left|\frac{C_{pol}C_{dep}}{C_{dep} + C_{pol}}\right|}\right)$$
(5)

By comparing each term of $1/A'_{\rm V}$ and $1/A_{\rm v}$, we can find $A'_{\rm V}$ > $A_{\rm V}$. Hence, $C_{\rm dep}$ can further enhance the subthreshold performance of the device attributed to the ferroelectric semiconducting property of α -In₂Se₃.

Moreover, dynamic polarization matching that affecting SS and ΔV was investigated by changing the sweep speed. 45 Figure 3e shows the bidirectional transfer curves for the slow (0.3 V/s), normal (0.9 V/s), and fast (2.9 V/s) sweep speed modes. It coherently exhibits counterclockwise ΔV , and the threshold voltage shifts to the negative direction as the sweep speed decreases because the gate bias polling time is reduced. The SS_{min} depending on the sweep speed for $V_{end} = 0$ and 2 V extracted from the bidirectional curve is shown in Figure 3f. The SS_{min} for each case was lower than 20 mV/dec; in particular, the SS_{min} decreased to 8 mV/dec at V_{end} = 2 V under a fast sweep speed mode. In addition, ΔV is dependent on the sweep speed that supports the polarization matching effect. The ΔV has been weakened in the fast sweep speed mode, as shown in Figure 3g. A benchmark plot for SS_{min} and ΔV versus the ON/OFF ratio compared with previously reported GaN-based transistors is shown in Figure 3h that confirms the record value of SS_{min} demonstrated by this work. The outstanding performance for both SS_{\min} and ΔV implies that the ferroelectric GaN/α-In₂Se₃ MOS-HEMT is a promising candidate for demonstrating a low power consumption toward neuromorphic applications. 5-7,9,11,13,46,47

Short-Term Plasticity of Ferroelectric GaN/α - In_2Se_3 MOS-HEMT. The heterointerface properties between α - In_2Se_3 - and AlGaN/GaN-based 2DEG enable the neuromorphic function of GaN/α - In_2Se_3 MOS-HEMT in STP. The read gate voltage was fixed as $V_{GS} = -9$ V, confirmed from the

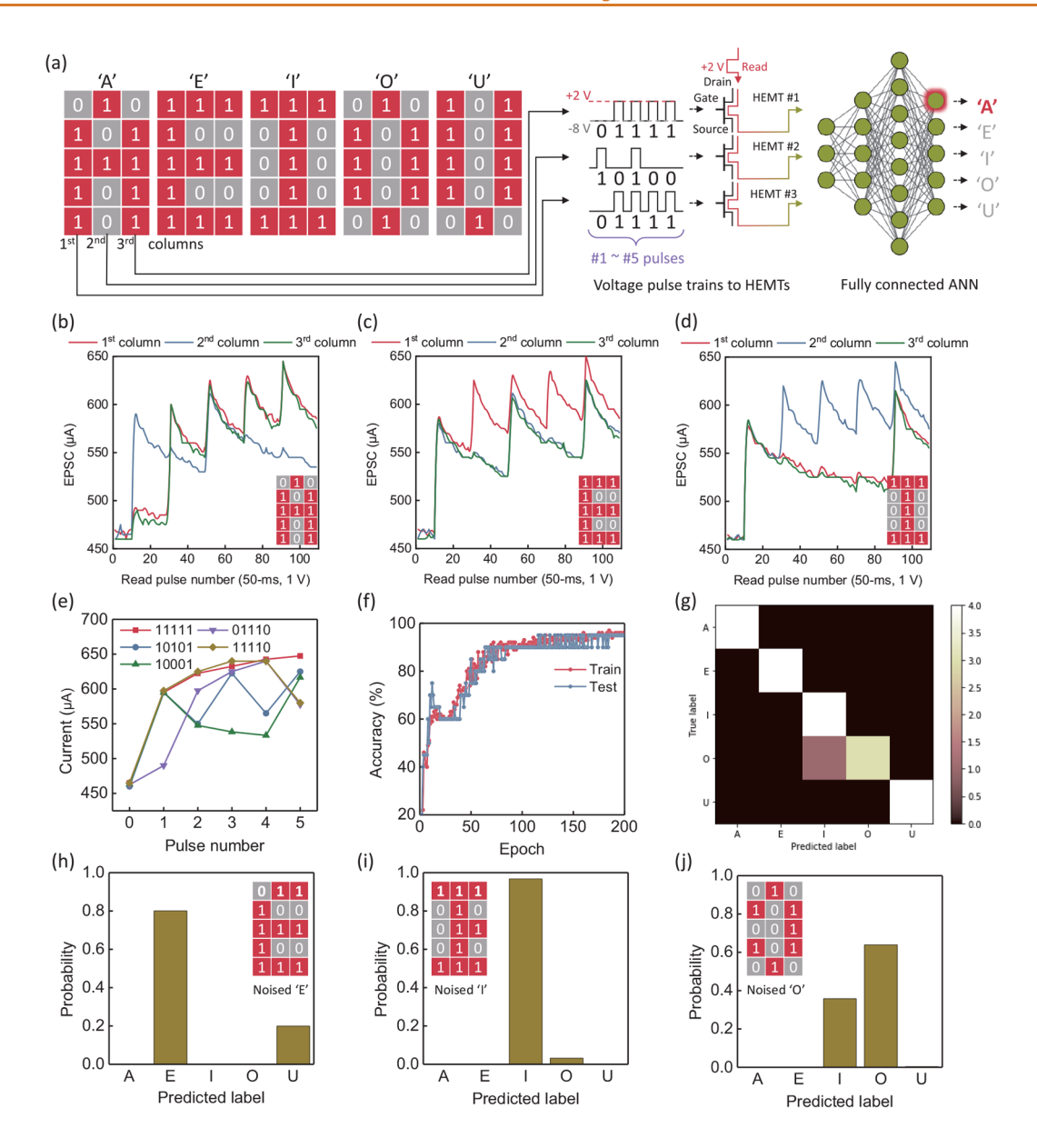


Figure 5. (a) Schematic illustration of vowel image classification (example of 'A'). 3×5 'A', 'E', 'I', 'O', and 'U' data sets are prepared, and the pixel intensities are converted to voltages ('0' \rightarrow -2 V and '1' \rightarrow +2 V). The accumulated pulses generate corresponding EPSCs at $V_D = 2$ V and $V_G = -6$ V. The readout EPSCs are normalized and fed into the pretrained fully connected layer (3–5–8–5 nodes) for classification. All pulses are 50 ms pulses with a 50% duty cycle. Experimental EPSC responses of letters (b) 'A', (c) 'E', and (d) 'I'. The EPSC peaks correspond to the '1' pixel intensity in each letter. (e) EPSC responses with respect to each pulse number. The current values corresponding to each pulse pattern are averaged. (f) Results of RC-based classification. For each train and test procedure, up to 97% and 95% accuracies are achieved, respectively. (g) Confusion matrix of vowel image classification. Inference results for noised (modifying one pixel) inputs, (h) 'E', (i) 'I', and (j) 'O'.

transfer curve (Figure S4). Figure 4a shows the EPSC responses for pulse widths of 1–500 ms, mimicking the biological STP. To compensate for the initial polarization caused by the AlGaN barrier layer, an initial setup pulse has been applied for 2 s. The EPSC showed a dependency on the pulse width, and the postsynaptic signal intensity has been increased as the wider pulse width has been applied. Figure 4b and c show the sequential EPSC for two pulses at a time interval of 10 ms and 100 μ s, respectively. Unlike the 10 ms interval, the shorter time interval (100 μ s) allows the accumulation of input spikes. The input spikes can be accumulated by increasing the pulse amplitude (Figure 4d).

Figure 4e shows the corresponding pair-pulse-facilitation (PPF) index plot. The time interval for extracting the parameters of the PPF index increased gradually from 10 ms to 500 ms. The maximum PPF index value was 114% at a time interval of 10 ms, whereas the minimum value was 100% at a time interval of 500 ms. Figure 4f shows the endurance times for the erase and program operations. Both operations were maintained for 5000 cycles without significant variations in the channel conductance ($G_{\rm DS}$).

Reservoir Computing. A complex circuit-based conventional recurrent neural network (RNN) has the disadvantage of noise in analog circuits entailing an output error. ⁴⁸ Notably,

RC operation is feasible via multistate dipole polarization of the GaN/α -In₂Se₃ MOS-HEMT that corresponds to the randomly distributed nodes in the reservoir layer. Furthermore, the coupled 2DEG channel allows for processing highfrequency input signals in the RC system. Here, based on the described electrical and neuromorphic characteristics above, we demonstrated the RC capability of the GaN/α -In₂Se₃ MOS-HEMT. Figure 5a shows a schematic of the RC system. We prepared 3 × 5 'A', 'E', 'I', 'O', and 'U' data sets for classification, and the pixel intensities of the data sets were converted to voltage amplitudes. Then, three 1 × 5 voltage pulses (corresponding to each letter) were applied to the gate electrode of the GaN/α -In₂Se₃ MOS-HEMT. The STP of the GaN/α -In₂Se₃ MOS-HEMT enabled the temporal encoding of input pulses without training. The input pulses in the letter images generated accumulated EPSC in a time domain (Figure 5b-d and Figure S5), which is then applied as an input to the fully connected neural network (FCNN). For example, the '1' pixel intensity generates the EPSC spike, whereas the '0' pixel intensity relaxes the EPSC intensity. As a result, the 3×5 input matrix is nonlinearly embedded into the distinguishable 3×1 vector (at the read pulse) as an input to the FCNN, offering the miniaturization of the FCNN model for faster classification. The corresponding readout currents for certain patterns are shown in Figure 5e. The continuous '1' input signals accumulated as increased EPSC intensity, whereas '0' signals relaxed the EPSC from the GaN/α -In₂Se₃ MOS-HEMT due to its STP. We have collected the encoded data and pretrained the FCNN (for more details, see the Methods section).

Figure 5f shows the training and test accuracies of the RC-based neural network. The accuracy converged to approximately 96% after the 50th epoch via the continuous optimization of the learning parameters, with a slight fluctuation during the first 50 epochs. Consequently, the training and test processes achieved accuracies of up to 97% and 95%, respectively. Figure 5g presents the confusion matrix for the classification. Although the classification accuracy of the 'O' is slightly degraded, the FCNN is robustly trained to infer noised images. For instance, noised 'E', 'I', and 'O' images are also classifiable via the FCNN, exhibiting the highest probability for the corresponding predictions, as shown in Figure 5h–j. The spontaneous STP behavior of the GaN/ α -In₂Se₃ MOS-HEMT can perform RC, encoding the input matrix as a vector for an effective classification task.

CONCLUSIONS

In this study, we have demonstrated ferroelectric GaN/ α -In₂Se₃ MOS-HEMTs with superior electrical performance by implementing a semiconducting α -In₂Se₃ layer to induce C_{dep} , which maximizes the effect of its ferroelectricity. The lowest SS (8 mV/dec) and large ΔV (2 V) were obtained owing to the polarization matching effect. The ferroelectric polarization and $\Delta\Phi_{\rm eff}$ were confirmed in the GaN/ α -In₂Se₃ MES-HEMT structure, which sufficiently controlled the 2DEG conductivity. In addition, the self-aligned etching process for the α -In₂Se₃ layer confines polarization in the vertical direction, which can further enhance ferroelectricity confirmed by both experiment and simulation using physics-based TCAD. Finally, we demonstrated the GaN/α-In₂Se₃ MOS-HEMT for neuromorphic computing applications by using its STP. RC was conducted using the measured and extracted characteristics of GaN/α -In₂Se₃ MOS-HEMT. The recognition accuracy for RC

reached 95% during the test process. Our study suggests that the GaN/α - In_2Se_3 MOS-HEMT is beneficial for demonstrating fast switching neuromorphic applications owing to the combination of semiconducting property of α - In_2Se_3 and the high carrier mobility of GaN HEMT. We believe the ferroelectric GaN/α - In_2Se_3 MOS-HEMTs have immense potential for processing high-frequency input signals.

METHOD

Device Fabrication. The AlGaN/GaN heterojunction was grown by metal-organic chemical vapor deposition on a 2 in. silicon substrate. It consists of a 3 nm GaN cap layer, 25 nm Al_{0.26}Ga_{0.74}N barriers, 1 nm AlN interlayer, 2 μ m GaN channel layer, and 1 μ m GaN buffer layer. The measured room-temperature Hall mobility and extracted sheet carrier concentrations were >1300 cm²/(V s) and $\sim 10^{13}$ cm⁻², respectively. Device fabrication was initiated by mesa isolation using a BCl₃/Cl₂-based inductively coupled plasma reactive ion etching system. A Ti/Au/Al/Ni/Au metal stack was deposited through e-beam evaporation, followed by rapid thermal annealing at 830 °C for 30 s in a N₂ environment for ohmic contact formation. Subsequently, 8 nm thick Al₂O₃ for the gate dielectric was deposited using an atomic layer deposition (ALD) system with trimethylaluminum and ozone precursors at a temperature of 450 °C. The α -In₂Se₃ flakes exfoliated from the α -In₂Se₃ bulk (HQ graphene) were then transferred as a ferroelectric layer. Subsequently, a Ni/Au (20 nm/50 nm) metal stack was deposited as a gate electrode through e-beam evaporation. Finally, the metal-gate aligned α-In₂Se₃ wet etching process was carried out for 60 s in an HCl-H2O2 = 1:5 mixture

Structural Characterizations. All electrical measurements were performed using a semiconductor parameter analyzer with a preamp (Keithley-4200A-SCS). The piezoelectric properties of α -In₂Se₃ were characterized using PFM (NX-10/Park Systems), and the thickness of the α -In₂Se₃ flake was verified using atomic force microscopy (XE-150/Park Systems). The Raman shift was measured using a Raman spectrometer (DXR2xi/Thermo).

Reservoir Computing Experiment. The pixel intensities of the letter images were encoded to voltage amplitudes (0 for -2 V and 1 for 2 V). The erase, read, and program voltages were -20, 1, and 2 V, respectively. All pulse widths were 50 ms. One hundred encoded data were collected (20 per letter) and divided into 80 training and 20 test images. A 3-5-8-5 FCNN was employed with ReLU activation layers (softmax for the last output). An RMSprop optimizer was employed with an initial time-decaying learning rate of 0.001.

ASSOCIATED CONTENT

Supporting Information

The Supporting Information is available free of charge at https://pubs.acs.org/doi/10.1021/acsnano.3c00187.

Operation principle and electrical properties of GaN/α -In₂Se₃ MES-HEMT; representative devices before and after gate-aligned α -In₂Se₃ etching process; influence of the area and thickness of α -In₂Se₃; electrical performance depending on sweep speed; transfer curve for STP measurement device; EPSC responses of reservoir computing (PDF)

AUTHOR INFORMATION

Corresponding Authors

Kyusang Lee — Department of Electrical and Computer Engineering, University of Virginia, Charlottesville, Virginia 22904, United States; Department of Material Science and Engineering, University of Virginia, Charlottesville, Virginia 22904, United States; Email: kl6ut@virginia.edu Geonwook Yoo — School of Electronic Engineering, Soongsil University, Seoul 06938, South Korea; oorcid.org/0000-0002-7826-9005; Email: gwyoo@ssu.ac.kr

Authors

- Jeong Yong Yang School of Electronic Engineering, Soongsil University, Seoul 06938, South Korea
- Minseong Park Department of Electrical and Computer Engineering, University of Virginia, Charlottesville, Virginia 22904, United States
- Min Jae Yeom School of Electronic Engineering, Soongsil University, Seoul 06938, South Korea
- Yongmin Baek Department of Electrical and Computer Engineering, University of Virginia, Charlottesville, Virginia 22904, United States
- Seok Chan Yoon School of Electronic Engineering, Soongsil University, Seoul 06938, South Korea
- Yeong Je Jeong School of Electronic Engineering, Soongsil University, Seoul 06938, South Korea
- Seung Yoon Oh School of Electronic Engineering, Soongsil University, Seoul 06938, South Korea

Complete contact information is available at: https://pubs.acs.org/10.1021/acsnano.3c00187

Notes

The authors declare no competing financial interest. $^{\perp}$ J.Y.Y., M.P., and M.J.Y. contributed equally to this work.

ACKNOWLEDGMENTS

This work was supported by National R&D Program through the National Research Foundation of Korea (NRF) funded by Ministry of Science and ICT (2020M3F3A2A01082593, 2021R1A4A1033155), and National Science Foundation (NSF) (Grant No. NSF ECCS-1942868). K.L. and M.P. were supported by the U.S. air force office of scientific research young investigator program under Grant FA9550-23-1-0159. The EDA tool was supported by the IC Design Education Center, Korea.

REFERENCES

- (1) Jayant Baliga, B. Trends in power semiconductor devices. *IEEE Trans. Electron Devices* **1996**, 43, 1717–1731.
- (2) Chau, R.; Datta, S.; Majumdar, A.Opportunities and challenges of III-V nanoelectronics for future high-speed, low-power logic applications. In *Technical Digest IEEE Compound Semiconductor Integrated Circuit Symposium, CSIC*; 2005; pp 17–20.
- (3) Dewey, G.; Hudait, M. K.; Lee, K.; Pillarisetty, R.; Rachmady, W.; Radosavljevic, M.; Rakshit, T.; Chau, R. Carrier transport in highmobility III-V quantum-well transistors and performance impact for high-speed low-power logic applications. *IEEE Electron Device Lett.* 2008, 29, 1094–1097.
- (4) Ueda, D. Review of compound semiconductor devices for RF power applications. In *in IEEE International Symposium on Power Semiconductor Devices and ICs (ISPSD)*; 2002.
- (5) Zhu, J.; Chen, L.; Jiang, J.; Lu, X.; Yang, L.; Hou, B.; Liao, M.; Zhou, Y.; Ma, X.; Hao, Y. Ferroelectric Gate AlGaN/GaN E-Mode HEMTs with High Transport and Sub-Threshold Performance. *IEEE Electron Device Lett.* **2018**, 39, 79–82.
- (6) Wu, C. H.; Han, P. C.; Liu, S. C.; Hsieh, T. E.; Lumbantoruan, F. J.; Ho, Y. H.; Chen, J. Y.; Yang, K. S.; Wang, H. C.; Lin, Y. K.; Chang, P. C.; Luc, Q. H.; Lin, Y. C.; Chang, E. Y. High-performance normally-OFF GaN MIS-HEMTs using hybrid ferroelectric charge trap gate stack (FEG-HEMT) for power device applications. *IEEE Electron Device Lett.* **2018**, 39, 991–994.

- (7) Chandrasekar, H.; Razzak, T.; Wang, C.; Reyes, Z.; Majumdar, K.; Rajan, S. Demonstration of Wide Bandgap AlGaN/GaN Negative-Capacitance High-Electron-Mobility Transistors (NC-HEMTs) Using Barium Titanate Ferroelectric Gates. *Adv. Electron. Mater.* **2020**, *6*, 2000074.
- (8) Li, G.; Li, X.; Liu, X.; Gao, A.; Zhao, J.; Yan, F.; Zhu, Q. Heteroepitaxy of $Hf_{0.5}Zr_{0.5}O_2$ ferroelectric gate layer on AlGaN/GaN towards normally off HEMTs. *Appl. Surf. Sci.* **2022**, *597*, 153709.
- (9) Wu, C.; Ye, H.; Shaju, N.; Smith, J.; Grisafe, B.; Datta, S.; Fay, P. Hf_{0.5}Zr_{0.5}O₂-Based Ferroelectric Gate HEMTs with Large Threshold Voltage Tuning Range. *IEEE Electron Device Lett.* **2020**, 41, 337–340.
- (10) Chen, L.; Wang, H.; Hou, B.; Liu, M.; Shen, L.; Lu, X.; Ma, X.; Hao, Y. Hetero-integration of quasi two-dimensional PbZr_{0.2}Ti_{0.8}O₃ on AlGaN/GaN HEMT and non-volatile modulation of two-dimensional electron gas. *Appl. Phys. Lett.* **2019**, *115*, 193505.
- (11) Song, W.; Li, Y.; Zhang, K.; Zou, X.; Wang, J.; Kong, Y.; Chen, T.; Jiang, C.; Liu, C.; Liao, L.; Liu, X. Steep Subthreshold Swing in GaN Negative Capacitance Field-Effect Transistors. *IEEE Trans. Electron Devices* **2019**, *66*, 4148–4150.
- (12) Ye, H.Ferroelectric-Gated GaN HEMTs for RF and mm-Wave Switch Applications. In 2022 International Symposium on VLSI Technology, Systems and Applications (VLSI-TSA) IEEE; 2022; p 12.
- (13) Chen, P. G.; Wei, Y. T.; Tang, M.; Lee, M. H. Experimental demonstration of ferroelectric gate-stack AlGaN/GaN-on-Si MOS-HEMTs with voltage amplification for power applications. *IEEE Trans. Electron Devices* **2014**, *61*, 3014–3017.
- (14) Zhao, D.; Lenz, T.; Gelinck, G. H.; Groen, P.; Damjanovic, D.; de Leeuw, D. M.; Katsouras, I. Depolarization of multidomain ferroelectric materials. *Nat. Commun.* **2019**, *10*, 2547.
- (15) Ni, K.; Sharma, P.; Zhang, J.; Jerry, M.; Smith, J. A.; Tapily, K.; Clark, R.; Mahapatra, S.; Datta, S. Critical Role of Interlayer in Hf_{0.5}Zr_{0.5}O₂ Ferroelectric FET Nonvolatile Memory Performance. *IEEE Trans. Electron Devices* **2018**, *65*, 2461–2469.
- (16) Toprasertpong, K.; Takenaka, M.; Takagi, S. Direct Observation of Interface Charge Behaviors in FeFET by Quasi-Static Split C-V and Hall Techniques: Revealing FeFET Operation. In in Technical Digest International Electron Devices Meeting, IEDM; 2019. (17) Si, M.; Saha, A. K.; Gao, S.; Qiu, G.; Qin, J.; Duan, Y.; Jian, J.; Niu, C.; Wang, H.; Wu, W.; Gupta, S. K.; Ye, P. D. A ferroelectric
- semiconductor field-effect transistor. *Nat. Electron* **2019**, *2*, 580–586. (18) Si, M.; Zhang, Z.; Chang, S. C.; Haratipour, N.; Zheng, D.; Li, J.; Avci, U. E.; Ye, P. D. Asymmetric Metal/ α -In₂Se₃/Si Crossbar Ferroelectric Semiconductor Junction. *ACS Nano* **2021**, *15*, 5689–
- (19) Wang, S.; Liu, L.; Gan, L.; Chen, H.; Hou, X.; Ding, Y.; Ma, S.; Zhang, D. W.; Zhou, P. Two-dimensional ferroelectric channel transistors integrating ultra-fast memory and neural computing. *Nat. Commun.* 2021, 12, 53.
- (20) Wang, X.; Yu, P.; Lei, Z.; Zhu, C.; Cao, X.; Liu, F.; You, L.; Zeng, Q.; Deng, Y.; Zhu, C.; Zhou, J.; Fu, Q.; Wang, J.; Huang, Y.; Liu, Z. Van der Waals negative capacitance transistors. *Nat. Commun.* **2019**, *10*, 3037.
- (21) Wang, X.; Zhu, C.; Deng, Y.; Duan, R.; Chen, J.; Zeng, Q.; Zhou, J.; Fu, Q.; You, L.; Liu, S.; Edgar, J. H.; Yu, P.; Liu, Z. Van der Waals engineering of ferroelectric heterostructures for long-retention memory. *Nat. Commun.* **2021**, *12*, 1109.
- (22) Singh, P.; Baek, S.; Yoo, H. H.; Niu, J.; Park, J. H.; Lee, S. Two-Dimensional CIPS-InSe van der Waal Heterostructure Ferroelectric Field Effect Transistor for Nonvolatile Memory Applications. *ACS Nano* **2022**, *16*, 5418–5426.
- (23) Jeong, K.; Lee, H.; Lee, C.; Wook, L. H.; Kim, H.; Lee, E.; Cho, M. H. Ferroelectric switching in GeTe through rotation of lone-pair electrons by Electric field-driven phase transition. *Appl. Mater. Today* **2021**, *24*, 101124.
- (24) Wu, J.; Chen, H. Y.; Yang, N.; Cao, J.; Yan, X.; Liu, F.; Sun, Q.; Ling, X.; Guo, J.; Wang, H. High tunnelling electroresistance in a ferroelectric van der Waals heterojunction via giant barrier height modulation. *Nat. Electron* **2020**, *3*, 466–472.

- (25) Yang, J. Y.; Yeom, M. J.; Lee, J.; Lee, K.; Park, C.; Heo, J.; Yoo, G. Reconfigurable Radio-Frequency High-Electron Mobility Transistors via Ferroelectric-Based Gallium Nitride Heterostructure. *Adv. Electron. Mater.* **2022**, *8*, 2101406.
- (26) Wang, Z.; Wu, H.; Burr, G. W.; Hwang, C. S.; Wang, K. L.; Xia, Q.; Yang, J. J. Resistive switching materials for information processing. *Nat. Reviews Materials* **2020**, *5*, 173–195.
- (27) Yao, P.; Wu, H.; Gao, B.; Tang, J.; Zhang, Q.; Zhang, W.; Yang, J. J.; Qian, H. Fully hardware-implemented memristor convolutional neural network. *Nature* **2020**, *577*, 641–646.
- (28) Liu, K.; Dang, B.; Zhang, T.; Yang, Z.; Bao, L.; Xu, L.; Cheng, C.; Huang, R.; Yang, Y. Multilayer Reservoir Computing Based on Ferroelectric α -In₂Se₃ for Hierarchical Information Processing. *Adv. Mater.* **2022**, 34, 2108826.
- (29) Sebastian, A.; le Gallo, M.; Khaddam-Aljameh, R.; Eleftheriou, E. Memory devices and applications for in-memory computing. *Nat. Nanotech* **2020**, *15*, 529–544.
- (30) Prezioso, M.; Merrikh-Bayat, F.; Hoskins, B. D.; Adam, G. C.; Likharev, K. K.; Strukov, D. B. Training and operation of an integrated neuromorphic network based on metal-oxide memristors. *Nature* **2015**, *521*, 61–64.
- (31) Park, See-On. et al. Experimental demonstration of highly reliable dynamic memristor for artificial neuron and neuromorphic computing. *Nat. Commun* 2022, *13*, 2888.
- (32) Li, Y.; Chen, C.; Li, W.; Mao, X.; Liu, H.; Xiang, J.; Nie, A.; Liu, Z.; Zhu, W.; Zeng, H. Orthogonal Electric Control of the Out-Of-Plane Field-Effect in 2D Ferroelectric α -In₂Se₃. *Adv. Electron Mater.* **2020**, *6*, 2000061.
- (33) Xue, F.; He, X.; Retamal, J. R. D.; Han, A.; Zhang, J.; Liu, Z.; Huang, J. K.; Hu, W.; Tung, V.; He, J. H.; Li, L. J.; Zhang, X. Gate-Tunable and Multidirection-Switchable Memristive Phenomena in a Van Der Waals Ferroelectric. *Adv. Mater.* **2019**, *31*, 1901300.
- (34) Vilaplana, R.; Parra, S. G.; Jorge-Montero, A.; Rodríguez-Hernández, P.; Munoz, A.; Errandonea, D.; Segura, A.; Manjón, F. J. Experimental and Theoretical Studies on α -In₂Se₃ at High Pressure. *Inorg. Chem.* **2018**, *57*, 8241–8252.
- (35) Gaskill, D. K., Brandt, C. D., Nemanich, R. J. III-Nitride, SiC and Diamond Materials for Electronic Devices. In *Materials Research Society Symposium*; April 8–12, 1996, San Francisco, CA, USA, Vol. 423; Materials Research Society: Pittsburgh, PA, 1996.
- (36) Bougrov, V.; Levinshtein, M. E.; Rumyantsev, S. L.; Zubrilov, A. In *Properties of Advanced Semiconductor Materials GaN, AlN, InN, BN, SiC, SiGe.* Bougrov, M. E.; Levinshtein; Rumyantsev, S. L.; Zubrilov, A., Eds.; Wiley: New York, 2001; pp 1–50.
- (37) Sang, L.; Liao, M.; Sumiya, M. A Comprehensive Review of Semiconductor Ultraviolet Photodetectors: From Thin Film to One-Dimensional Nanostructures. *Sensors* **2013**, *13*, 10482–10518.
- (38) Grabowski, S. P.; Schneider, M.; Nienhaus, H.; Mönch, W.; Dimitrov, R.; Ambacher, O.; Stutzmann, M. Electron affinity of Al_xGa1-_xN (0001) surfaces. *Appl. Phys. Lett.* **2001**, 78, 2503.
- (39) Hosseini, S. M.; Aliabad, H. A. R.; Kompany, A. Influence of La on electronic structure of α -Al₂O₃ high k-gate from first principles. *Ceram. Int.* **2005**, *31*, 671–675.
- (40) Iwasaki, H.; Sudoh, K. Electron tunneling through an Al_2O_3 thin film on NiAl(110) in scanning tunneling microscopy. *Japanese Journal of Applied Physics* **2002**, *41*, 7496.
- (41) Yang, J. Y.; Yeom, M. J.; Park, Y.; Heo, J.; Yoo, G. Ferroelectric α -In₂Se₃ Wrapped-Gate β -Ga₂O₃ Field-Effect Transistors for Dynamic Threshold Voltage Control. *Adv. Electron Mater.* **2021**, 7, 2100306.
- (42) Si, M.; Su, C. J.; Jiang, C.; Conrad, N. J.; Zhou, H.; Maize, K. D.; Qiu, G.; Wu, C. T.; Shakouri, A.; Alam, M. A.; Ye, P. D. Steepslope hysteresis-free negative capacitance MoS₂ transistors. *Nat. Nanotech* **2018**, *13*, 24–28.
- (43) Cao, W.; Banerjee, K. Is negative capacitance FET a steep-slope logic switch? *Nat. Commun.* **2020**, *11*, 196.
- (44) Choi, K. B.; Woo, S. Y.; Kang, W. M.; Lee, S.; Kim, C. H.; Bae, J. H.; Lim, S.; Lee, J. H. A split-gate positive feedback device with an

- integrate-and-fire capability for a high-density low-power neuron circuit. Front Neurosci 2018, 12, 704.
- (45) Wang, H.; Yang, M.; Huang, Q.; Zhu, K.; Zhao, Y.; Liang, Z.; Chen, C.; Wang, Z.; Zhong, Y.; Zhang, X.; Huang, R. New Insights into the Physical Origin of Negative Capacitance and Hysteresis in NCFETs. In in Technical Digest International Electron Devices Meeting, IEDM; 2019.
- (46) Chen, L.; Ma, X.; Zhu, J.; Hou, B.; Song, F.; Zhu, Q.; Zhang, M.; Yang, L.; Hao, Y. Polarization Engineering in PZT/AlGaN/GaN High-Electron-Mobility Transistors. *IEEE Trans. Electron Devices* **2018**, *65*, 3149–3155.
- (47) Cui, P.; Lin, G.; Zhang, J.; Zeng, Y. Sub-60 mV/decade Switching via Hot Electron Transfer in Nanoscale GaN HEMTs. *IEEE Electron Device Lett.* **2020**, *41*, 1185–1188.
- (48) Zhong, Y.; Tang, J.; Li, X.; et al. A memristor-based analogue reservoir computing system for real-time and power-efficient signal processing. *Nat. Electron* **2022**, *5*, 672–681.

□ Recommended by ACS

Reconfigurable Two-Dimensional Air-Gap Barristors

Guangqi Zhang, Yang Wei, et al.

FEBRUARY 27, 2023

ACS NANO READ ☑

Dual-Gate All-Electrical Valleytronic Transistors

Shen Lai, Wei-bo Gao, et al.

JANUARY 03, 2023

NANO LETTERS

READ 🗹

$\label{eq:continuous} \textbf{Dual-Channel WS}_2/WSe_2 \ \textbf{Heterostructure with Tunable Graphene Electrodes}$

Hanul Kim, Gil-Ho Kim, et al.

JANUARY 20, 2023

ACS APPLIED ELECTRONIC MATERIALS

READ [7

Light-Tunable Polarity and Erasable Physisorption-Induced Memory Effect in Vertically Stacked InSe/SnS₂ Self-Powered Photodetector

Yue Zhao, Han-Chun Wu, et al.

SEPTEMBER 26, 2022

ACS NANO

READ 🗹

Get More Suggestions >